

A three-dimensional non-isothermal Ginzburg–Landau phase-field model for shape memory alloys

R Dhote^{1,3}, M Fabrizio², R Melnik³ and J Zu¹

¹ Mechanical and Industrial Engineering, University of Toronto, 5 King's College Road, Toronto, ON, M5S3G8, Canada

² Department of Mathematics, University of Bologna, Piazza di Porta S. Donato 5, I-40126 Bologna, Italy

³ The MS2Discovery Interdisciplinary Research Institute & M²NeT Laboratory, Wilfrid Laurier University, Waterloo, ON, N2L3C5, Canada

E-mail: rakesh.dhote@mail.utoronto.ca

Received 12 March 2014, revised 18 August 2014

Accepted for publication 15 September 2014

Published 12 November 2014

Abstract

In this paper, a macroscopic three-dimensional non-isothermal model is proposed for describing hysteresis phenomena and phase transformations in shape memory alloys (SMAs). The model is of phase-field type and is based on the Ginzburg–Landau theory. The hysteresis and phase transformations are governed by the kinetic phase evolution equation using the scalar order parameter, laws of conservation of the momentum and energy and a nonlinear coupling of the stress, the strain and the order parameter in a differential form. One of the important features of the model is that the phase transformation is governed by the stress tensor, as opposed to the transformation strain tensor typically used in the literature. The model takes into account different properties of austenite and martensite phases based on the compliance tensor as a function of the order parameter and stress. Representative numerical simulations on an SMA specimen reproduce hysteretic behaviors observed experimentally in the literature.

Keywords: shape memory alloy, non-isothermal, Ginzburg–Landau theory, phase-field model

(Some figures may appear in colour only in the online journal)

1. Introduction

Over the past few decades, shape memory alloys (SMAs) have attracted increasing attention from physicists, engineers and applied mathematicians because of their complex microstructures and interesting thermomechanical hysteretic behaviors. The SMAs exhibit two unique hysteresis behaviors, namely, a shape memory effect and pseudoelasticity at lower and higher temperatures (with respect to the threshold temperature). These behaviors are caused by the underlying atomic rearrangements from a symmetric configuration (called the austenite (A) phase) to other configurations of lower symmetry (called the martensite (M) phases). Under mechanical and thermal loadings, the atomic rearrangement results in a macroscopic deformation of an SMA specimen due to diffusionless transformations. The simultaneous presence of high-stress and high-strain properties for SMAs makes them suitable candidates for actuator and sensor use in a wide range of products in automotive, aerospace, medicine and bioengineering applications [1–6].

Several modeling approaches have been proposed for describing hysteretic behaviors in SMAs. A comprehensive overview of different SMA models can be found in, e.g. [3, 7, 8]. The approaches based on phenomenology, phase diagrams, micromechanics, crystal plasticity, phase-field models, etc. have been described in detail in [9–12] and the references therein. In this paper, we focus on the phase-field (PF) model approach. This approach provides a unified framework to describe temperature-induced and stress-induced transformations. Several different PF models have been proposed in [13–30]. They differ in the free energy description, selection of order parameters (OPs), model formulation and numerical approaches.

Inspired by the phase-field modeling of ferroelectric materials, Falk [13] applied the Landau–Devonshire theory in order to describe martensitic transformations (MTs) in SMAs by defining the shear strain as an OP. Later, Wang and Khachaturyan [31] proposed a three-dimensional (3D) continuum stochastic-field kinetic model by defining the transformation-induced elastic strain as OPs in order to predict the MTs. Curnoe and Jacobs [32], Lookman *et al* [33] and Bouville and Ahluwalia [26, 27] used an approach of defining elastic strain components as the OPs. Polynomial-based phenomenological descriptions of the free energy as a function of OPs and their gradients are used to describe the dynamics of phase transformations. One of the previous notable contributions to the PF theory is the Landau free energy proposed by Levitas *et al* [19–21]. The free energy yields a description of the thermomechanical properties of different phases using the tensorial OPs. The strain tensor is decomposed into an elastic component and a transformational component, where the latter is a function of the OPs. The model employs the same number of phase evolution equations as there are martensitic variants considered during the phase transformation. Later, Mahapatra and Melnik [23, 24] derived a non-isothermal model based on the free energy developed by Levitas *et al* [19–21] by modifying the multivariant framework to obtain strongly coupled thermomechanical models with the essential properties of frame indifference and material symmetry.

Recently, Berti *et al* [34, 35], Grandi *et al* [36], Maraldi *et al* [37] and Dhote *et al* [30] developed a non-isothermal thermodynamic framework for modeling MTs in SMAs. The macroscopic frameworks for 1D and 3D models have been developed on the basis of a simplified version of the free energy proposed by Levitas *et al* [19]. Here, we are particularly interested in the 3D model proposed by Dhote *et al* [30]. One of the important features of the 3D model within the non-isothermal framework is the use of a scalar phase OP instead of the tensorial OPs used earlier in the literature [19–21]. The application of this approach reduces the problem size by limiting the number of phase evolution equations to 1, instead of considering separate equations for each crystallographic variant [19–21]. This results in a simple model which is amenable to an efficient numerical implementation. The other highlights of the model

are (i) the rate-dependent constitutive equations coupling the stress, strain and phase order parameter, (ii) the description of the phase transformation based on the stress tensor and (iii) the phase-dependent properties obtained by incorporating the compliance tensor based on the local phase value and stress.

In this paper, the 3D non-isothermal model is implemented and examples in a 2D setting of study of the SMA behavior are provided. In our earlier publication [30], the numerical experiments were conducted on the model by numerically solving the kinetic phase evolution and constitutive equation in 1D and the pseudo-2D case driven by stress loading, but without incorporating the conservation laws of momentum and energy. The model is now studied here incorporating the full thermomechanical coupling and phase evolution equations. In addition, the model is simulated with the material properties of the Ni₅₅Ti₄₅ specimen [28, 38].

The paper is organized as follows. In section 2, a 3D non-isothermal model is described using the kinetic phase evolution, nonlinear couplings of the stress, strain and order parameter and laws of conservation of the momentum and energy. In section 3, representative simulations on a rectangular SMA specimen are described in detail and studied under different loading conditions. Finally, the conclusions are given in section 4.

2. The 3D non-isothermal phase-field model

The fully coupled thermomechanical PF model is developed to describe the nonlinear hysteretic response of SMAs. We define the OP ϕ to describe the austenite ($\phi = 0$) and martensite ($\phi = 1$) phases. Here we do not distinguish between different variants of martensites. This is a different approach as compared to a multivariant OP approach (e.g. see [19–21]). It facilitates the development of a simpler model which is computationally tractable, but at the expense of distinction between different martensitic variants individually. In the following section, the governing equations of the phase evolution and the conservation laws for momentum and energy are described.

2.1. The phase evolution equation

In order to derive a phase evolution equation, we choose a free energy functional that has minima at $\phi = 0$ and $\phi = 1$ with no distinction between martensitic variants. The free energy functional Ψ based on the Ginzburg–Landau potential is given by

$$\Psi = \frac{\kappa}{2} |\nabla \phi|^2 - \frac{1}{2} (\boldsymbol{\sigma} \boldsymbol{\lambda} \cdot \boldsymbol{\sigma}) + \frac{\ell}{2} \left\{ \theta_0 \mathcal{F}(\phi) + \left(\hat{\theta} - \frac{\epsilon_0}{\ell} \frac{\boldsymbol{\sigma} \cdot \boldsymbol{\sigma}}{|\boldsymbol{\sigma}|} \right) \mathcal{G}(\phi) \right\}, \quad (1)$$

where κ is the Ginzburg constant, $\boldsymbol{\sigma}$ is the stress tensor, $\boldsymbol{\lambda}$ is the compliance tensor, ℓ is the latent heat of the phase transition, θ_0 and $\hat{\theta}$ are the temperatures and ϵ_0 is the equivalent transformation strain. The potentials $\mathcal{F}(\phi)$ and $\mathcal{G}(\phi)$ are the 2–3–4 polynomial functions of ϕ defined as

$$\mathcal{F}(\phi) = \frac{1}{2}\phi^2 - \frac{2}{3}\phi^3 + \frac{1}{4}\phi^4 + \beta(\phi^2 - \phi), \quad \mathcal{G}(\phi) = \begin{cases} 0 & \text{if } \phi < 0, \\ \frac{1}{2}\phi^2 - \frac{1}{4}\phi^4 & \text{if } 0 \leq \phi \leq 1, \\ \frac{1}{4} & \text{if } \phi > 1. \end{cases} \quad (2)$$

Here, the constant β is a very small perturbing term added to accommodate slope variations in the regime of instability ($0 < \beta \ll 1$) as described in [35]. We define

$$\hat{\theta} = \begin{cases} \theta - \theta_A & \text{if } \theta > \theta_A, \\ 0 & \text{if } \theta \leq \theta_A, \end{cases} \quad (3)$$

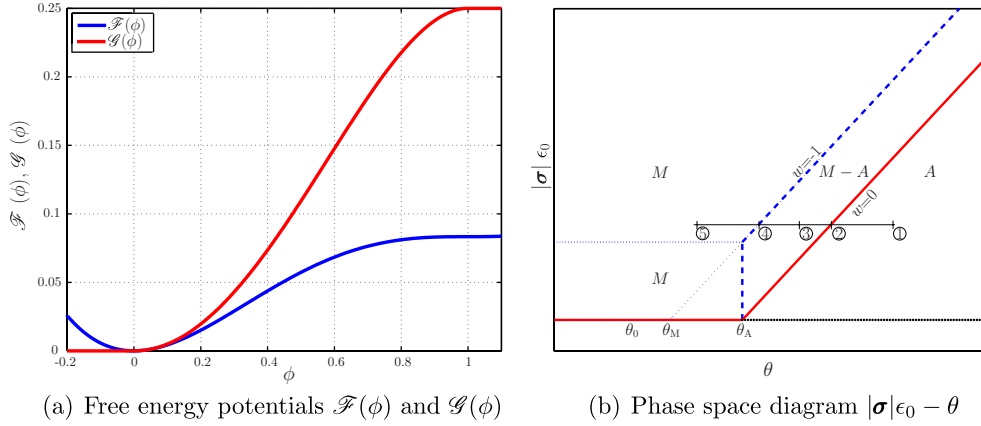


Figure 1. Free energy \mathcal{E} and $|\sigma|\epsilon_0$ - θ phase space plot.

where $\theta_A > \theta_0$. The temperature θ_M is defined as $\theta_M = \theta_A - \theta_0$. The free energy potentials $\mathcal{F}(\phi)$ and $\mathcal{G}(\phi)$, and the $|\sigma|\epsilon_0$ - θ phase space diagram, are plotted in figures 1(a) and (b), respectively.

The two-well free energy functional \mathcal{E} , defining the minimum at $\phi = 0$ and $\phi = 1$, is mapped to the potentials \mathcal{F} and \mathcal{G} as

$$\mathcal{E} = \mathcal{F} + w\mathcal{G}, \quad (4)$$

where w is the function of temperature and stress defined as

$$w = \frac{1}{\theta_0} \left(\hat{\theta} - \frac{\epsilon_0}{\ell} \frac{\sigma \cdot \sigma}{|\sigma|} \right). \quad (5)$$

The two-well free energy functional \mathcal{E} is plotted for different values of w in figure 2. The phase in the domain adheres to the following rules:

- $w > 0$: functional \mathcal{E} has a minimum at $\phi = 0$;
- $w < -1$: functional \mathcal{E} has a minimum at $\phi = 1$;
- $-1 < w < 0$: functional \mathcal{E} has metastable states at $\phi = 0$ and/or $\phi = 1$.

Thus the lines $w = -1$ and $w = 0$ represent the critical threshold for the disappearance of the minimum at $\phi = 0$ and that at $\phi = 1$, respectively [35]. The M, A and M-A regions are shown in figure 1(b). The numbers ①–⑤ in figure 1(b) correspond schematically to the functional \mathcal{E} shown in figure 2(b).

We closely follow [30, 35] for deriving the governing equations. For consistency and completeness, the highlights of the main derivation are summarized as follows.

The temporal evolution of the OP is described by the first-order kinetic time-dependent Ginzburg–Landau (TDGL) equation. The TDGL equation is stated as follows:

$$\gamma \frac{\partial \phi}{\partial t} = -\frac{\delta \Psi}{\delta \phi} + \nabla \cdot \left(\frac{\delta \Psi}{\delta \nabla \phi} \right), \quad (6)$$

where γ is the relaxation parameter and δ defines the functional derivative.

On substituting equation (1) into equation (6) and mathematical manipulation, we obtain the phase evolution equation as

$$\gamma \frac{\partial \phi}{\partial t} = \kappa \Delta \phi - \frac{\ell}{2} \left\{ \theta_0 \frac{\partial \mathcal{F}(\phi)}{\partial \phi} + \left(\hat{\theta} - \frac{\epsilon_0}{\ell} \frac{\sigma \cdot \sigma}{|\sigma|} \right) \frac{\partial \mathcal{G}(\phi)}{\partial \phi} \right\}. \quad (7)$$

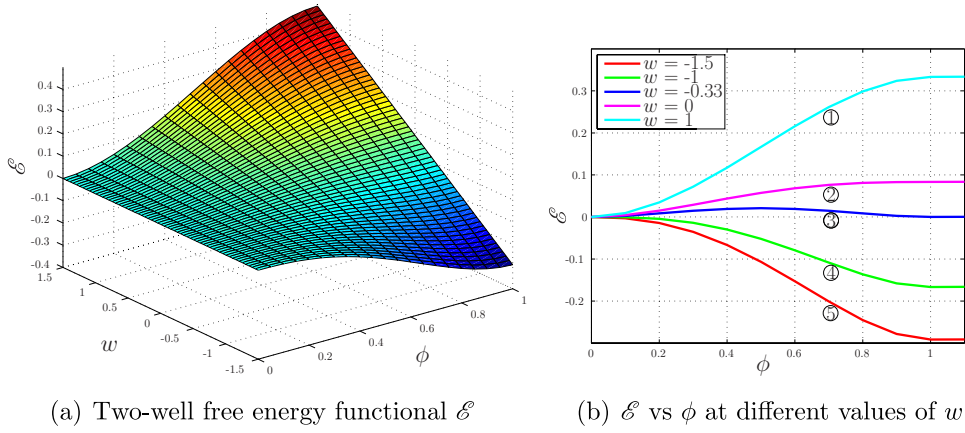


Figure 2. Two-well free energy function \mathcal{E} .

2.2. The structural equations

The structural equations are described by using the kinematic relationship, the appropriate constitutive equation and the law of conservation of momentum.

2.2.1. The kinematic relationship. The model is developed on the basis of isotropic material properties and a small strain framework. The infinitesimal Cauchy–Lagrange strain tensor ϵ is defined as

$$\epsilon = \frac{1}{2} (\nabla \mathbf{u} + \nabla \mathbf{u}^T), \quad (8)$$

where \mathbf{u} is the displacement vector and \mathbf{x} is the spatial coordinate vector.

2.2.2. The constitutive relationship. The relationship between the stress and the strain is defined using the constitutive equations. In the case of the phase-changing systems, the constitutive equations are modified to account for the phase transformation in order to describe the hysteresis. Thus the constitutive equations not only relate the σ and ϵ , but also the ϕ . The common methodology used to achieve this is the decomposition of strain into the elastic and phase transformation components [14, 19–21, 23, 28, 37]. We too follow this methodology; however, we take into account the different forms of the dependences of the compliance on ϕ and σ . In this case, the constitutive equation is of differential form [30, 35], given as

$$\dot{\epsilon} = \lambda^{1/2}(\sigma, \phi) \frac{\partial}{\partial t} (\lambda^{1/2}(\sigma, \phi) \sigma) + \epsilon_0 \frac{\sigma}{|\sigma|} \dot{\phi}. \quad (9)$$

The first and second terms on the right-hand side in equation (9) represent the elastic and transformational components of the strain in a differential form. The compliance tensor λ accommodates the properties of both austenite and martensite phases on the basis of the OP value and the stress [19]. In the general 3D case, it is defined as

$$\lambda(\sigma, \phi) = \lambda_2(\phi) + \lambda_3(\phi) \sigma + \lambda_4(\phi) \sigma \cdot \sigma, \quad (10)$$

where λ_2 , λ_3 and λ_4 are the tensors of fourth, sixth and eighth orders, respectively. A point to be noted is that in equation (9) the phase transformation is governed by the stress tensor σ as opposed to the transformation strain tensor described, e.g. in [14, 19–21, 23, 28, 37].

2.2.3. Conservation of the momentum. The structural balance is governed by the law of conservation of momentum. It reads as

$$\rho \ddot{\mathbf{u}} = \nabla \cdot \boldsymbol{\sigma} + \rho \mathbf{f}, \quad (11)$$

where ρ is the density and \mathbf{f} is the body force.

2.3. The thermal equation and thermodynamic consistency

The free energy ψ can be expressed in the terms of the internal energy e and entropy η as

$$\psi = e - \theta \eta. \quad (12)$$

According to the first law of thermodynamics, the balance of energy is written as

$$\rho \dot{e}(\boldsymbol{\sigma}, \phi, \theta) = \mathcal{P}_m^i + \mathcal{P}_\phi^i - \nabla \cdot \mathbf{q} + r, \quad (13)$$

where \mathcal{P}_m^i is the internal mechanical power, \mathcal{P}_ϕ^i is the internal order structure power, \mathbf{q} is the heat flux defined as $\mathbf{q} = -k \nabla \theta$ and r is the external heat source. \mathcal{P}_m^i is defined as

$$\mathcal{P}_m^i = \boldsymbol{\sigma} \cdot \dot{\boldsymbol{\epsilon}}, \quad (14)$$

and \mathcal{P}_ϕ^i is obtained by multiplying equation (7) by $\dot{\phi}$ and following the approach of [34]:

$$\mathcal{P}_\phi^i = \gamma \dot{\phi}^2 + \frac{\kappa}{2} \frac{d}{dt} (|\nabla \phi|^2) + \frac{\ell}{2} \left\{ \theta_0 \dot{\mathcal{F}}(\phi) + \left(\hat{\theta} - \frac{\epsilon_0}{\ell} \frac{\boldsymbol{\sigma} \cdot \boldsymbol{\sigma}}{|\boldsymbol{\sigma}|} \right) \dot{\mathcal{G}}(\phi) \right\}. \quad (15)$$

In order to prove the consistency of the above model with the second law of thermodynamics, the Clausius–Duhem inequality has to be satisfied. Thus,

$$\dot{\eta} \geq -\nabla \cdot \left(\frac{\mathbf{q}}{\theta} \right) + \frac{r}{\theta}. \quad (16)$$

Using equations (12)–(15) and (16), this inequality is reduced to

$$\dot{\psi} + \dot{\theta} \eta \leq -\frac{\mathbf{q}}{\theta} \cdot \nabla \theta + \frac{1}{2} \frac{d}{dt} (\lambda(\boldsymbol{\sigma}, \phi) \boldsymbol{\sigma} \cdot \boldsymbol{\sigma}) + \gamma \dot{\phi}^2 + \kappa \nabla \phi \cdot \nabla \dot{\phi} + \frac{\ell}{2} \theta_0 \dot{\mathcal{F}}(\phi) + \frac{\ell}{2} \hat{\theta} \dot{\mathcal{G}}(\phi). \quad (17)$$

Under the assumption that the free energy ψ is a function of the variables $\phi, \nabla \phi, \boldsymbol{\sigma}, \theta$, equation (17) can be written as

$$\begin{aligned} & \left(\eta + \frac{\partial \psi}{\partial \theta} \right) \dot{\theta} + \left(\frac{\partial \psi}{\partial \phi} - \frac{\ell}{2} \theta_0 \mathcal{F}'(\phi) - \frac{\ell}{2} \hat{\theta} \mathcal{G}'(\phi) \right) \dot{\phi} + \left(\frac{\partial \psi}{\partial \nabla \phi} - \kappa \nabla \phi \right) \cdot \nabla \dot{\phi} \\ & + \left(\frac{\partial \psi}{\partial \boldsymbol{\sigma}} - \lambda(\boldsymbol{\sigma}, \phi) \boldsymbol{\sigma} \right) \cdot \dot{\boldsymbol{\sigma}} - \gamma \dot{\phi}^2 + \frac{\mathbf{q}}{\theta} \cdot \nabla \theta \leq 0. \end{aligned} \quad (18)$$

The above inequality is satisfied for arbitrariness of $\dot{\phi}, \nabla \dot{\phi}, \dot{\boldsymbol{\sigma}}, \dot{\theta}$ under the following constitutive relations:

$$\eta = -\frac{\partial \psi}{\partial \theta}, \quad \frac{\partial \psi}{\partial \phi} = \frac{\ell}{2} \left[\theta_0 \mathcal{F}'(\phi) + \hat{\theta} \mathcal{G}'(\phi) \right], \quad \frac{\partial \psi}{\partial \nabla \phi} = \kappa \nabla \phi, \quad \frac{\partial \psi}{\partial \boldsymbol{\sigma}} = \lambda(\boldsymbol{\sigma}, \phi) \boldsymbol{\sigma}, \quad (19)$$

where \mathcal{F}' and \mathcal{G}' are derivatives with respect to the OP ϕ .

Substituting equation (19) in (18) leads to

$$\frac{k}{\theta} |\nabla \theta|^2 + \gamma \dot{\phi}^2 \geq 0, \quad (20)$$

thus proving the thermodynamic consistency with the positivity of the thermal conductivity k .

The relations in equation (19) enforce the following representation of the free energy:

$$\psi = \psi_0(\theta) + \frac{1}{2} (\lambda(\boldsymbol{\sigma}, \phi) \boldsymbol{\sigma} \cdot \boldsymbol{\sigma}) + \frac{\kappa}{2} |\nabla \phi|^2 + \frac{\ell}{2} \left[\theta_0 \mathcal{F}(\phi) + \hat{\theta} \mathcal{G}(\phi) \right], \quad (21)$$

where we choose ψ_0 as

$$\psi_0(\theta) = -\frac{c}{2\theta_c}\theta^2. \quad (22)$$

Now, the expression for the internal energy e in equation (12) can be simplified as follows:

$$e = \frac{c}{2\theta_c}\theta^2 + \frac{1}{2}(\lambda(\sigma, \phi)\sigma \cdot \sigma) + \frac{\kappa}{2}|\nabla\phi|^2 + \frac{\ell}{2}\left[\theta_0\mathcal{F}(\phi) + (\hat{\theta} - \theta\hat{\theta}')\mathcal{G}(\phi)\right], \quad (23)$$

where $\hat{\theta}'$ is the derivative with respect to the temperature θ .

On differentiating equation (23) with respect to time and equating it to the right-hand side of equation (13), we obtain the heat equation as

$$\frac{c}{\theta_c}\theta\dot{\theta} - \frac{\ell}{2}\theta\left[\mathcal{G}(\phi)\hat{\theta}''\dot{\theta} + \hat{\theta}'\dot{\mathcal{G}}(\phi)\right] - \gamma\dot{\phi}^2 = k\Delta\theta + r. \quad (24)$$

Defining $\hat{\theta}'$ and $\hat{\theta}''$ as the Heaviside function H and the Dirac-delta function δ_d , the equation (24) can be written explicitly as

$$\frac{c}{\theta_c}\theta\dot{\theta} - \frac{\ell}{2}\theta\left[\mathcal{G}(\phi)\delta_d\dot{\theta} + H\dot{\mathcal{G}}(\phi)\right] - \gamma\dot{\phi}^2 = k\Delta\theta + r. \quad (25)$$

2.4. The system of equations and boundary conditions

Now, we summarize all the governing partial differential equations and constitutive relations for the above model as

$$\gamma\frac{\partial\phi}{\partial t} = \kappa\Delta\phi - \frac{\ell}{2}\left\{\theta_0\frac{\partial\mathcal{F}(\phi)}{\partial\phi} + \left(\hat{\theta} - \frac{\epsilon_0}{\ell}\frac{\sigma \cdot \sigma}{|\sigma|}\right)\frac{\partial\mathcal{G}(\phi)}{\partial\phi}\right\}, \quad (26.1)$$

$$\rho\ddot{\mathbf{u}} = \nabla \cdot \boldsymbol{\sigma} + \rho\mathbf{f}, \quad (26.2)$$

$$\frac{c}{\theta_c}\theta\dot{\theta} - \frac{\ell}{2}\theta\left[\mathcal{G}(\phi)\delta_d\dot{\theta} + H\dot{\mathcal{G}}(\phi)\right] - \gamma\dot{\phi}^2 = k\Delta\theta + r. \quad (26.3)$$

The kinematic relations and constitutive equation are described as follows:

$$\boldsymbol{\epsilon} = \frac{1}{2}[\nabla\mathbf{u} + \nabla\mathbf{u}^T], \quad (27.1)$$

$$\dot{\boldsymbol{\epsilon}} = \lambda^{1/2}(\sigma, \phi)\frac{\partial}{\partial t}(\lambda^{1/2}(\sigma, \phi)\boldsymbol{\sigma}) + \epsilon_0\frac{\boldsymbol{\sigma}}{|\boldsymbol{\sigma}|}\dot{\mathcal{G}}(\phi), \quad (27.2)$$

along with the boundary conditions (refer to figure 3 for the boundary nomenclature)

$$\begin{aligned} \mathbf{n} \cdot \nabla\phi|_{\Gamma} = 0, \quad \mathbf{u}|_{\Gamma_1} = \mathbf{0}, \quad \mathbf{n} \cdot \boldsymbol{\sigma}|_{\Gamma_{2,3}} = 0, \quad \mathbf{n} \cdot \boldsymbol{\sigma}|_{\Gamma_4} = \bar{\boldsymbol{\sigma}} \quad \text{or} \quad \mathbf{u}|_{\Gamma_4} = \bar{\mathbf{u}}, \\ \mathbf{n} \cdot \nabla\theta|_{\Gamma} = h(\theta - \theta_{\text{ext}}), \end{aligned} \quad (28)$$

where h is the heat transfer coefficient, θ_{ext} is the external environment temperature and $\bar{\boldsymbol{\sigma}}$ and $\bar{\mathbf{u}}$ are the stress-based and displacement-based ramp loadings, respectively. The initial conditions are defined as

$$\phi(x, 0) = \phi_0(x), \quad \mathbf{u}(x, 0) = \mathbf{u}_0(x), \quad \dot{\mathbf{u}}(x, 0) = \dot{\mathbf{u}}_0(x), \quad \theta(x, 0) = \tilde{\theta}_0(x) = \theta_{\text{ext}}(x). \quad (29)$$

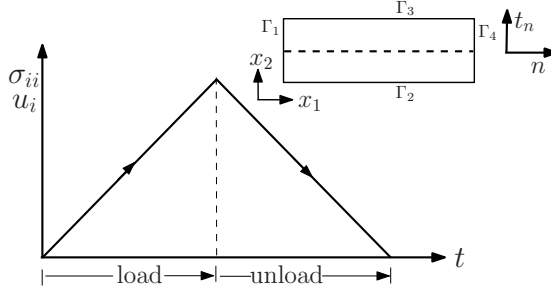


Figure 3. Schematic of boundary nomenclature and the ramp loading and unloading.

2.5. The weak formulation

Let $\Omega \subset \mathbb{R}^d$ be an open set in the d -dimensional space ($d = 2, 3$) defined by the coordinate system \mathbf{x} . The boundary is denoted by Γ and its outward normal by \mathbf{n} . As the constitutive equations are assumed in differential form in equations (27.1) and (27.2), we solve them along with equations (26.1)–(26.3). The weak formulations of equations (26.1)–(26.3) and equations (27.1) and (27.2) are derived by multiplying the equations with weighting functions $\{\Phi, U, \Sigma, \Theta\}$ and transforming them by using integration by parts. Let X denote both the trial solution and the weighting function spaces, which are assumed to be identical. Let $(\cdot, \cdot)_\Omega$ denote the L^2 inner product with respect to the domain Ω . The variational formulation is stated as follows. Find the solution $\mathbf{S} = \{\phi, \mathbf{u}, \boldsymbol{\sigma}, \theta\} \in X$ such that $\forall \mathbf{W} = \{\Phi, U, \Sigma, \Theta\} \in X$, we have $B(\mathbf{W}, \mathbf{S}) = 0$, with

$$\begin{aligned}
 B(\mathbf{W}, \mathbf{S}) = & (\Phi, \gamma \dot{\phi})_\Omega + (\nabla \cdot \Phi, \kappa \nabla \cdot \phi)_\Omega + \left(\Phi, \frac{\ell}{2} \theta_0 \frac{\partial \mathcal{F}}{\partial \phi} \right)_\Omega + \left(\Phi, \frac{\ell}{2} \hat{\theta} \frac{\partial \mathcal{G}}{\partial \phi} \right)_\Omega \\
 & - \left(\Phi, \epsilon_0 \frac{\boldsymbol{\sigma} \cdot \boldsymbol{\sigma}}{|\boldsymbol{\sigma}|} \frac{\partial \mathcal{G}}{\partial \phi} \right)_\Omega + (U, \rho \ddot{\mathbf{u}})_\Omega + (\nabla \cdot U, \boldsymbol{\sigma})_\Omega - (U, \rho \mathbf{f})_\Omega + (\Sigma, \dot{\epsilon})_\Omega \\
 & - \left(\Sigma, \lambda^{1/2} \frac{\partial}{\partial t} (\lambda^{1/2} \boldsymbol{\sigma}) \right)_\Omega - \left(\Sigma, \epsilon_0 \frac{\boldsymbol{\sigma}}{|\boldsymbol{\sigma}|} \dot{\mathcal{G}}(\phi) \right)_\Omega + \left(\Theta, c \frac{\theta}{\theta_c} \dot{\theta} \right)_\Omega - \left(\Theta, \frac{\ell}{2} \theta \dot{\theta} \delta_d \mathcal{G} \right)_\Omega \\
 & - \left(\Theta, \frac{\ell}{2} \theta H \dot{\mathcal{G}} \right)_\Omega - (\Theta, \gamma \dot{\phi}^2)_\Omega + (\nabla \cdot \Theta, k \nabla \cdot \theta)_\Omega - (\Theta, r)_\Omega \\
 & - (\Phi, \kappa \nabla \phi \cdot \mathbf{n})_\Gamma - (U, \boldsymbol{\sigma} \cdot \mathbf{n})_\Gamma - (\Theta, k \nabla \theta \cdot \mathbf{n})_\Gamma.
 \end{aligned} \tag{30}$$

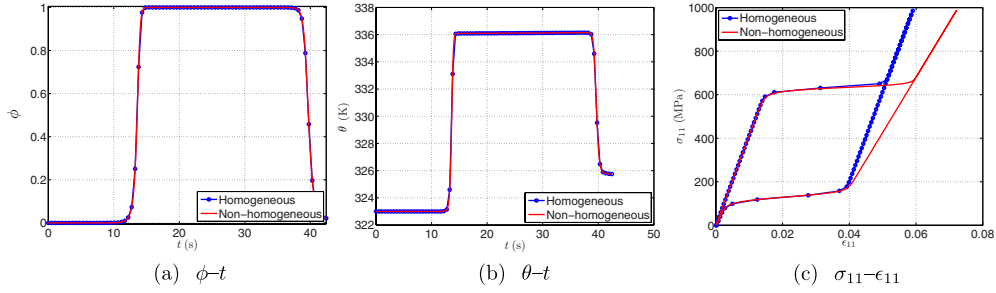
Equations (30) have been implemented in a weak finite element formulation in the Comsol Multiphysics software [39].

3. Numerical experiments

We exemplify the SMA hysteretic behavior in a 2D setting. A rectangular specimen of domain $\Omega = [0, l_x] \times [0, l_y]$ is chosen for the numerical simulations. We assume the plane stress formulation, considering that the thickness is small as compared to the other dimensions. For simplicity, we adopt the quasistatic approximation under the assumption that the timescales of the thermal dynamics and phase evolution phenomenon are larger than the stress wave timescale [28, 37]. We neglect the nonlinear effect of the λ_3 and λ_4 compliance tensors. We assume that no external body and thermal loads are applied during the simulation. The

Table 1. Material parameters of polycrystalline Ni₅₅Ti₄₅.

λ_A	λ_M	ℓ	ϵ_0	θ_A	μ		
$2.5 \times 10^{-11} \text{ Pa}^{-1}$	$3.57 \times 10^{-11} \text{ Pa}^{-1}$	10^6 Pa K^{-1}	0.14	288.5 K	0.33		
γ	θ_M	θ_0	θ_c	c	k	κ	
$80 \times 10^5 \text{ Pa s}$	273 K	212.7 K	296 K	$3.2 \times 10^6 \text{ Pa K}^{-1}$	$18 \text{ W m}^{-1} \text{ K}^{-1}$	0.15 N	

**Figure 4.** Average ϕ , θ evolution and σ_{11} – ϵ_{11} curves for phase-dependent compliance properties.

phase-dependent compliance tensor λ_2 takes the form

$$\lambda_2 = \lambda_A \begin{bmatrix} (1 + \Xi\phi) & -\mu(1 + \Xi\phi) & 0 \\ -\mu(1 + \Xi\phi) & (1 + \Xi\phi) & 0 \\ 0 & 0 & (1 + \mu)(1 + \Xi\phi) \end{bmatrix}, \quad (31)$$

where $\Xi = (\lambda_M - \lambda_A)/\lambda_A$. The material properties of an Ni₅₅Ti₄₅ specimen [28, 38] are summarized in table 1. Some of the parameter values have been assumed to reproduce the hysteretic properties of the material. The equivalent transformation strain $\epsilon_0 = 0.14$ during the simulations is selected. Although the ϵ_0 value falls in the finite strain regime, we have not considered it in the current formulation. The interested readers are referred to [40, 41] and references therein for further details on the finite strain phase-field models. The governing equations are first rescaled and then implemented in the weak formulation. The results are later converted back to the dimensional form.

3.1. The SMA behavior under stress-controlled loadings

In the following subsections, we describe the results of the simulations that have been carried out on a rectangular domain with $l_x = 0.1$ m and $l_y = 0.008$ m, to show the ability of the model to reproduce the SMA hysteretic behavior under the stress-controlled loading. It should be noted that the stress-controlled loading often leads to uniform nucleation in a specimen, which is different from the nonuniform nucleation observed during a displacement-controlled loading [28, 38]. Hence, a stress drop is not observed during the phase nucleation in a stress-controlled loading [37]. In this paper, we do not consider the defects and their associated oscillating stress fields. The interested readers are referred to [42, 43] for more details.

3.1.1. The phase-dependent properties. First, a simulation was carried out to show the effect of phase-dependent properties on the hysteretic behavior of SMAs. Two cases are considered:

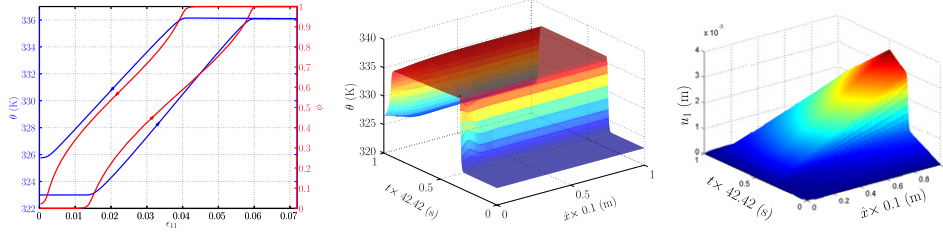


Figure 5. Plot of (a) the ϵ_{11} – θ – ϕ loop and the central axial line arc length (\hat{x}) extrusion plot for the (b) θ and (c) displacement u_1 evolution.

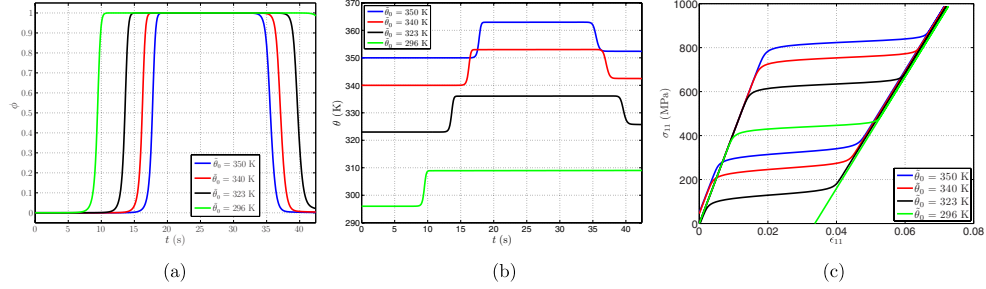


Figure 6. Average ϕ , θ evolution and σ_{11} – ϵ_{11} curve starting with different values of $\tilde{\theta}_0$.

first, an SMA specimen with equal elastic compliances of the two phases ($\lambda_M = \lambda_A$); and second, an SMA specimen with local phase-dependent compliance of the austenite and martensite phases ($\lambda_M \neq \lambda_A$). The loadings are carried out with $\dot{\sigma}_{11} = 46.47 \text{ MPa s}^{-1}$ starting with the initial temperature $\tilde{\theta}_0 = 323 \text{ K}$ for both cases. The average ϕ , θ evolution and σ_{11} – ϵ_{11} curve calculated over the area of the specimen are shown in figure 4. The ϕ and θ evolve identically in the two cases. However, the effect of local phase-dependent compliance is apparent on the σ_{11} – ϵ_{11} curve. Figure 5(a) indicates the thermal hysteresis θ – ϵ_{11} and phase evolution ϕ – ϵ_{11} loops for the local phase-dependent compliance case. The central axial line (refer to the dashed line on the domain in figure 3) arc length (\hat{x}) extrusion plots of θ and the axial displacement u_1 are shown in figures 5(b) and (c). Note that the phase-dependent compliance has been reported experimentally [1, 3, 38]. Due to the higher compliance of the martensite phase, as compared to the austenite phase, the area under the σ_{11} – ϵ_{11} curve is large, thus causing more energy dissipation in the local phase-dependent properties. In all of the subsequent simulations, we use the local phase-dependent compliance properties of the phases.

3.1.2. The SMA behavior at different initial temperatures. Next, the hysteretic response of an SMA specimen is studied starting with different initial temperatures $\tilde{\theta}_0$ ranging from 296 K to 350 K, using the axial stress rate $\dot{\sigma}_{11} = 46.47 \text{ MPa s}^{-1}$. The average ϕ , θ evolution and σ_{11} – ϵ_{11} curve are shown in figure 6. At the lower initial temperature ($\tilde{\theta}_0 = 296 \text{ K}$), the shape memory effect is observed with remnant strain at the end of the unloading. The pseudoelastic behavior, with fully recoverable strain, is observed at higher $\tilde{\theta}_0$. As $\tilde{\theta}_0$ increases, higher axial stress is required for the start of the phase transformation, thus offsetting the σ_{11} – ϵ_{11} curve toward a higher value. The area under the σ_{11} – ϵ_{11} curve remains constant. These results are consistent with the results reported in the literature [28, 37, 38].

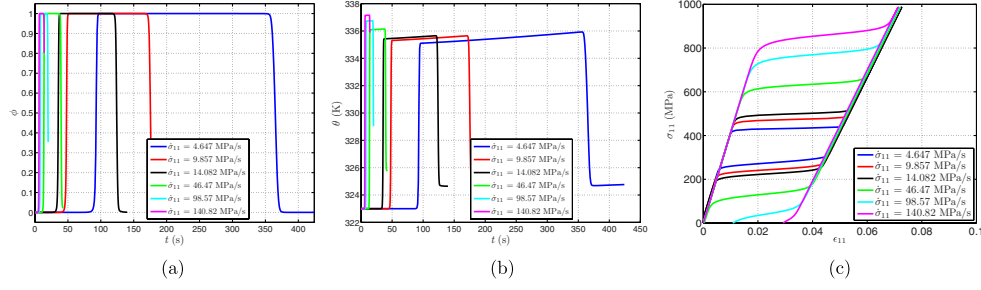


Figure 7. Average ϕ , θ evolution and σ_{11} – ϵ_{11} curve for different loading rates $\dot{\sigma}_{11}$.

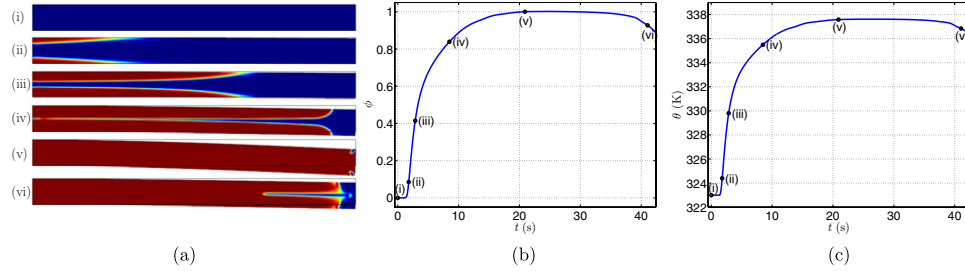


Figure 8. Bending loading evolution of (a) ϕ , (b) average ϕ and (c) average θ . Markers in parts (b) and (c) correspond to different time t instants in (a). Displacements u are superimposed on ϕ in (a) for better clarity. The phase evolution plots (i)–(v) in (a) correspond to the loading path and (vi) is for near the end of unloading.

3.1.3. The SMA behavior at different stress rates. Next, simulations were conducted on an SMA specimen with different axial $\dot{\sigma}_{11}$ loading rates ranging between 4.647 MPa s^{-1} and $140.82 \text{ MPa s}^{-1}$ and starting with the initial temperature $\tilde{\theta}_0 = 323 \text{ K}$. The average ϕ , θ evolution and σ_{11} – ϵ_{11} curve are shown in figure 7. With increase in $\dot{\sigma}_{11}$, the phase transformation starts at higher stress values. As the loading rate increases, the heat generated during the exothermic (A \rightarrow M) process causes the internal temperature of the specimen to increase due to there being insufficient time for heat transfer to the environment. During the (M \rightarrow A) process, the heat is absorbed due to the endothermic nature of the phase transformation. The dissipation energy (the area of the hysteresis loop in the σ_{11} – ϵ_{11} curve) increases with increasing $\dot{\sigma}_{11}$. It is observed that with increase in $\dot{\sigma}_{11}$, the slope of phase transformation increases. The above behaviors have been experimentally observed [38].

3.1.4. The SMA behavior under bending loading. A simulation is conducted on an SMA specimen by applying the constraint $u = \mathbf{0}$ on the boundary Γ_1 and applying tangential ramp stress loading on the boundary Γ_4 in the x_2 direction corresponding to $\dot{\sigma}_{yy} = 19.9 \text{ MPa s}^{-1}$. The initial temperature at the start of the simulation is $\tilde{\theta}_0 = 323 \text{ K}$. The phase evolution ϕ snapshots are plotted at different times in figure 8(a). The blue and red colors represent A and M phases, respectively. During the loading phase, the tensile stress is generated on the top fiber and the compressive stress on the bottom fiber of the specimen. Nonhomogeneous regions of A and M domains, separated by domain walls, are formed. As the model formulation does not account for different martensite variants, the M regions on the top and bottom coalesce near the end of loading. The average ϕ and θ plots are presented in figures 8(b)–(c). The formation of

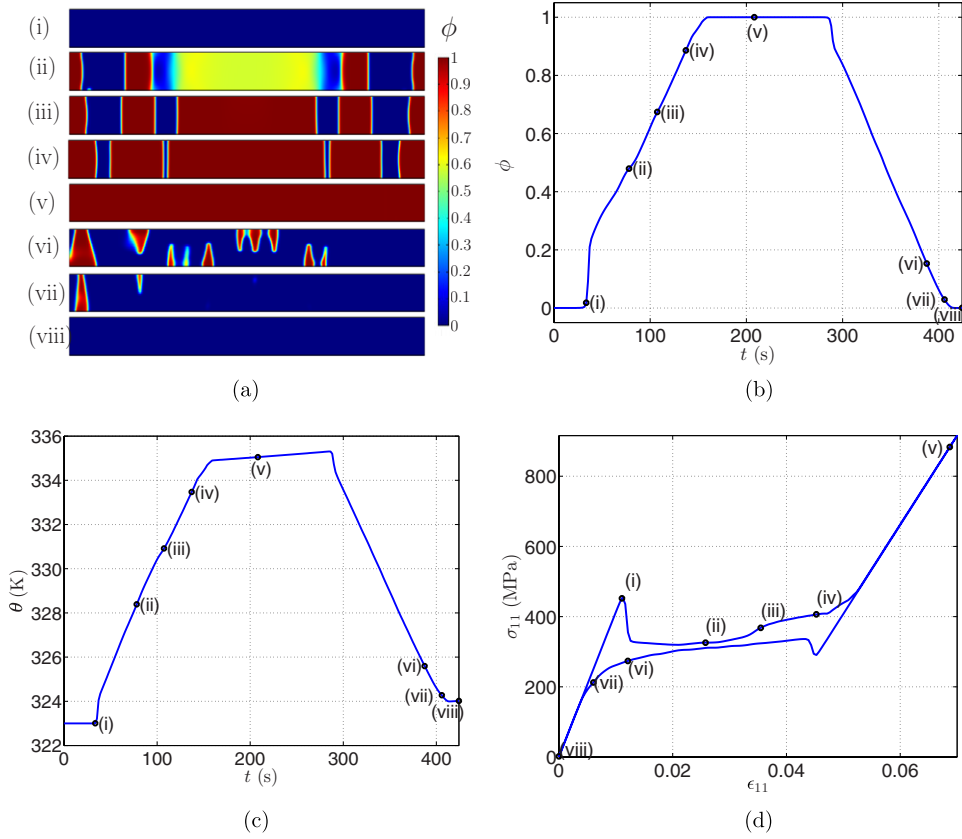


Figure 9. Displacement-controlled loading: evolution of (a) ϕ , (b) average ϕ , (c) average θ and (d) average $\sigma_{11}-\epsilon_{11}$. Markers in parts (b), (c) and (d) correspond to different time t instants in (a). The phase evolution plots (i)–(v) in (a) correspond to the loading and plots (vi)–(viii) to the unloading path.

M regions on the top and bottom edges has been experimentally reported by Rejzner *et al* [44] for SMAs subjected to pure bending loading.

3.2. The SMA behavior under displacement-controlled loading

In the previous sections, we studied the behavior of an SMA specimen under stress-controlled loading. Here, we now load the SMA specimen ($l_x = 0.1$ m and $l_y = 0.01$ m) in the x_1 direction with a displacement-controlled ramp loading. The specimen, initially at $\tilde{\theta}_0 = 323$ K, is constrained on the boundary Γ_1 with $\mathbf{u} = \mathbf{0}$ and a ramp displacement corresponding to $\dot{\epsilon}_{11} = 3.3 \times 10^{-4}$ s is applied on the boundary Γ_4 .

Time evolution snapshots of phase ϕ at different times are plotted in figure 9(a). The martensite nucleates at different locations in the domain, causing nonhomogeneous regions of A and M. As the loading progresses, different martensite regions coalesce to form a homogeneous M region. At the end of unloading, the domain returns back to the A phase. Average $\phi-t$, $\theta-t$ and $\sigma_{11}-\epsilon_{11}$ results obtained during the loading–unloading process are presented in figures 9(b)–(d). Exothermic and endothermic natures of the phase evolution are observed during the (A \rightarrow M) and (M \rightarrow A) transformations, respectively.

4. Conclusions

A macroscale non-isothermal 3D model has been developed for describing nonlinear phase-dependent hysteretic behaviors in SMAs. The model is thermodynamically consistent with a rate-dependent constitutive relationship, and the conservation laws of thermal and mechanical physics, in conjunction with a kinetic phase evolution equation. In its description of the phase transformations, the model is based on the stress tensor and utilizes a scalar order parameter.

Representative numerical simulations for the stress-controlled loadings illustrate that the phase-dependent compliance properties improve the pseudoelastic nonlinear hysteretic description. The tensile tests on SMA specimens with different initial temperatures, as well as loading rates, elucidate the model's ability to capture efficiently the thermomechanical behavior and phase kinetics. The model successfully reproduces experimentally observed SMA behaviors reported in the literature.

Acknowledgment

RD and RM were supported by NSERC and CRC programs, Canada. RM also acknowledges TÜBITAK for support.

References

- [1] Otsuka K and Wayman C 1998 *Shape Memory Materials* (Cambridge: Cambridge University Press)
- [2] Kohl M 2004 *Shape Memory Microactuators* (Berlin: Springer)
- [3] Lagoudas D 2008 *Shape Memory Alloys: Modeling and Engineering Applications* (London: Springer)
- [4] Miyazaki S, Fu Y Q and Huang W M 2009 *Thin Film Shape Memory Alloys: Fundamentals and Device Applications* (Cambridge: Cambridge University Press)
- [5] Ozbulut O, Hurlebaus S and DesRoches R 2011 Seismic response control using shape memory alloys: a review *J. Intell. Mater. Syst. Struct.* **22** 1531–49
- [6] Elahinia M, Hashemi M, Tabesh M and Bhaduri S 2012 Manufacturing and processing of NiTi implants: a review *Prog. Mater. Sci.* **57** 911–46
- [7] Khandelwal A and Buravalla V 2009 Models for Shape memory alloy behavior: an overview of modelling approaches *Int. J. Struct. Changes Solids—Mech. Appl.* **1** 111–48
- [8] Lagoudas D, Brinson L and Patoor E 2006 Shape memory alloys: II. Modeling of polycrystals *Mech. Mater.* **38** 430–62
- [9] Birman V 1997 Review of mechanics of shape memory alloy structures *Appl. Mech. Rev.* **50** 629–45
- [10] Smith R 2005 *Smart material systems: model development* vol 32 (Philadelphia, PA: SIAM)
- [11] Paiva A and Savi M A 2006 An overview of constitutive models for shape memory alloys. *Math. Prob. Eng.* **56876** 1–30
- [12] Mamivand M, Zaeem M and El Kadiri H 2013 A review on phase field modeling of martensitic phase transformation *Comput. Mater. Sci.* **77** 304–11
- [13] Falk F 1980 Model free energy, mechanics, and thermodynamics of shape memory alloys *Acta Metall.* **28** 1773–80
- [14] Khachaturian A 1983 *Theory of Structural Transformations in Solids* (New York: Wiley)
- [15] Melnik R, Roberts A and Thomas K 1999 Modelling dynamics of shape-memory-alloys via computer algebra *Proc. SPIE Math. Control Smart Struct.* **3667** 290–301
- [16] Melnik R, Roberts A and Thomas K A 2002 Computing dynamics of Copper-based SMA via center manifold reduction models *Comput. Mater. Sci.* **18** 255–68
- [17] Artemev A, Jin Y and Khachaturyan A G 2001 Three-dimensional phase field model of proper martensitic transformation *Acta Mater.* **49** 1165–77

- [18] Chen L 2002 Phase field models for microstructure evolution *Annu. Rev. Mater. Res.* **32** 113–40
- [19] Levitas V and Preston D 2002 Three-dimensional Landau theory for multivariant stress-induced martensitic phase transformations: I. austenite \leftrightarrow martensite *Phys. Rev. B* **66** 1–9
- [20] Levitas V and Preston D 2002 Three-dimensional Landau theory for multivariant stress-induced martensitic phase transformations: II. Multivariant phase transformations, stress space analysis *Phys. Rev. B* **66** 1–15
- [21] Levitas V, Preston D and Lee D 2003 Three-dimensional Landau theory for multivariant stress-induced martensitic phase transformations: III. Alternative potentials, critical nuclei, kink solutions, and dislocation theory *Phys. Rev. B* **68** 1–24
- [22] Ahluwalia R, Lookman T and Saxena A 2006 Dynamic strain loading of cubic to tetragonal martensites *Acta Mater.* **54** 2109–20
- [23] Mahapatra D and Melnik R 2006 Finite element analysis of phase transformation dynamics in shape memory alloys with a consistent Landau–Ginzburg free energy model *Mech. Adv. Mater. Struct.* **13** 443–55
- [24] Mahapatra D and Melnik R 2007 Finite element approach to modelling evolution of 3D shape memory materials *Math. Comput. Simul.* **76** 141–8
- [25] Wang L and Melnik R 2007 Finite volume analysis of nonlinear thermo-mechanical dynamics of shape memory alloys *Heat Mass Transfer* **43** 535–46
- [26] Bouville M and Ahluwalia R 2008 Microstructure and mechanical properties of constrained shape memory alloy nanograins and nanowires *Acta Mater.* **56** 3558–67
- [27] Bouville M and Ahluwalia R 2009 Phase field simulations of coupled phase transformations in Ferroelastic–ferroelastic nanocomposites *Phys. Rev. B* **79** 094110
- [28] Grandi D, Maraldi M and Molari L 2012 A macroscale phase-field model for shape memory alloys with non-isothermal effects: influence of strain rate and environmental conditions on the mechanical response *Acta Mater.* **60** 179–91
- [29] Dhote R, Melnik R and Zu J 2012 Dynamic thermo-mechanical coupling, size effects in finite shape memory alloy nanostructures *Comput. Mater. Sci.* **63** 105–17
- [30] Dhote R, Fabrizio M, Melnik R and Zu J 2013 Hysteresis phenomena in shape memory alloys by non-isothermal Ginzburg–Landau models *Commun. Nonlinear Sci. Numer. Simul.* **18** 2549–61
- [31] Wang Y and Khachaturyan A 1997 Three-dimensional field model and computer modeling of martensitic transformations *Acta Mater.* **45** 759–73
- [32] Curnoe S and Jacobs A 2000 Twin wall of proper cubic–tetragonal ferroelastics *Phys. Rev. B* **62** 11925–8
- [33] Lookman T, Shenoy S R, Rasmussen K, Saxena A and Bishop A R 2003 Ferroelastic dynamics and strain compatibility *Phys. Rev. B* **67** 24114
- [34] Berti V, Fabrizio M and Grandi D 2010 Phase transitions in shape memory alloys: a non-isothermal Ginzburg Landau model *Physica D* **239** 95–102
- [35] Berti V, Fabrizio M and Grandi D 2010 Hysteresis and phase transitions for one-dimensional and three-dimensional models in shape memory alloys *J. Math. Phys.* **51** 062901
- [36] Grandi D, Maraldi M and Molari L 2012 A macroscale phase-field model for shape memory alloys with non-isothermal effects: influence of strain rate and environmental conditions on the mechanical response *Acta Mater.* **60** 179–91
- [37] Maraldi M, Molari L and Grandi D 2012 A non-isothermal phase-field model for shape memory alloys: numerical simulations of superelasticity and shape memory effect under stress-controlled conditions *J. Intell. Mater. Syst. Struct.* **23** 1083–92
- [38] Zhang X, Feng P, He Y, Yu T and Sun Q 2010 Experimental study on rate dependence of macroscopic domain and stress hysteresis in NiTi shape memory alloy strips *Int. J. Mech. Sci.* **52** 1660–70
- [39] Comsol Multiphysics Software, Version 4.2. (www.comsol.com)
- [40] Levitas V 2013 Phase-field theory for martensitic phase transformations at large strains *Int. J. Plast.* **49** 85–118
- [41] Levin V, Levitas V, Zingerman K and Freiman E 2013 Phase-field simulation of stress-induced martensitic phase transformations at large strains *Int. J. Solids Struct.* **50** 2914–28

- [42] Levitas V and Lee D 2007 Athermal resistance to interface motion in the phase-field theory of microstructure evolution *Phys. Rev. Lett.* **99** 245701
- [43] Lloveras P, Castán T, Porta M, Planes A and Saxena A 2010 Thermodynamics of stress-induced ferroelastic transitions: influence of anisotropy and disorder *Phys. Rev. B* **81** 214105
- [44] Rejzner J, Lexcellent C and Raniecki B 2002 Pseudoelastic behaviour of shape memory alloy beams under pure bending: experiments and modelling *Int. J. Mech. Sci.* **44** 665–86